Materials Advances

PAPER

View Article Online
View Journal | View Issue

Open Access Article. Published on 28 August 2025. Downloaded on 4/29/2026 2:04:37 AM.
This article is licensed under a Creative Commons Attribution-NonCommercial 3.0 Unported Licence.

Cite this: *Mater. Adv.*, 2025, **6**, 6978

Received 9th July 2025,
Accepted 26th August 2025

DOI: 10.1039/d5ma00731c

rsc.li/materials-advances

Carbazole-linked through-space TADF emitters for OLEDs: tuning photophysics *via* molecular architecture and exciton dynamics

Sanyam, Nishi Tejiyan and Anirban Mondal*

Thermally activated delayed fluorescence (TADF) offers a promising route to highly efficient organic light-emitting diodes (OLEDs), yet conventional D–A–D and A–D–A architectures often suffer from conformational flexibility, leading to multiple singlet excited states and enhanced non-radiative decay. These effects compromise both emission efficiency and color purity. While multi-resonant TADF (MR-TADF) systems provide improved rigidity, their planar structures favor π–π stacking, causing aggregation-induced quenching (ACQ). This study presents a molecular design strategy integrating a carbazole unit as a rigid, non-planar bridge to mitigate intramolecular rotation and suppress ACQ by disrupting parallel stacking. A set of 21 such D–A–D and A–D–A type molecules was computationally designed and analyzed. The optimized structures exhibit spatially separated frontier orbitals, resulting in small singlet–triplet energy gaps (ΔE_{ST}), fast radiative and reverse intersystem crossing rates, and near-unity photoluminescence quantum yields (PLQYs). Exciton dynamics simulations further confirm efficient TADF behavior, while molecular dynamics trajectories reveal conformational stability and through-space charge transfer characteristics. Notably, **A1–D3–A1** achieves an exceptionally small ΔE_{ST} of 0.001 eV and the highest k_{TADF} of 1.34×10^6 s^{-1}, enabling rapid triplet harvesting, while **D1–A2–D3** combines high oscillator strength with efficient TADF dynamics. These results demonstrate that subtle architectural tuning can yield substantial performance improvements, highlighting carbazole-bridged TADF emitters as a pathway toward stable, high-efficiency OLED materials.

1. Introduction

Thermally activated delayed fluorescence (TADF) compounds have emerged as a promising class of organic materials for applications in organic light-emitting diodes (OLEDs) and advanced display technologies.[1–6] Based on their underlying electronic architectures, TADF emitters are broadly classified into two categories: (i) conventional donor–acceptor–donor (D–A–D) or acceptor–donor–acceptor (A–D–A) structures,[2,7–9] and (ii) multi-resonant TADF (MR-TADF) systems.[10–12] In the case of D–A–D or A–D–A type molecules, the highest occupied molecular orbital (HOMO) is typically localized on the donor units, while the lowest unoccupied molecular orbital (LUMO) is situated on the acceptor moieties. This pronounced spatial separation of frontier orbitals leads to a small singlet–triplet energy gap ($\Delta E_{ST} \approx 0$ eV), which promotes efficient reverse intersystem crossing (RISC) and enables the upconversion of non-emissive triplet excitons into delayed fluorescence.[13–16] Despite these advantages, D–A–D and related architectures often suffer from intrinsic limitations due to flexible single bonds connecting the donor and acceptor fragments. Such conformational freedom facilitates intramolecular rotations that open up non-radiative decay pathways and lead to a distribution of conformers with varying emission characteristics. As a result, these systems frequently exhibit diminished emission efficiency and poor color purity, posing challenges for their integration into high-performance OLED devices.[17–21]

Multi-resonant TADF materials have been developed to overcome the limitations of flexible D–A–D-type TADF emitters. In these systems, the charge-transfer process is confined within a rigid and fully conjugated molecular framework, effectively suppressing intramolecular rotations and minimizing non-radiative decay pathways. MR-TADF molecules typically integrate boron atoms—featuring empty p-orbitals—as electron acceptors and heteroatoms such as nitrogen, oxygen, or sulfur as electron donors, all embedded within a single planar aromatic scaffold. The structural rigidity of this design not only enhances photophysical stability but also leads to impressive external quantum efficiencies (EQEs) and photoluminescence quantum yields (PLQYs), as demonstrated by numerous recent MR-TADF emitters developed across various research groups.[10–12]

Department of Chemistry, Indian Institute of Technology Gandhinagar, Gujarat, 382355, India. E-mail: amondal@iitgn.ac.in

© 2025 The Author(s). Published by the Royal Society of Chemistry

Open Access Article. Published on 28 August 2025. Downloaded on 4/29/2026 2:04:37 AM.
This article is licensed under a Creative Commons Attribution-NonCommercial 3.0 Unported Licence.

However, the enhanced rigidity of MR-TADF systems also introduces new challenges. In particular, the closer spatial proximity of the donor and acceptor fragments often leads to increased overlap between the HOMO and LUMO orbitals, thereby enlarging the ΔE_{ST} and potentially reducing RISC efficiency. Moreover, the inherently planar geometries of MR-TADF molecules facilitate strong π–π interactions in the solid state or at high concentrations, leading to aggregation-caused quenching (ACQ) and reduced device performance.[22,23] These π–π stacking interactions typically form H-type aggregates—characterized by nearly perpendicular arrangements of molecular planes—which hinder radiative decay from the first singlet excited state (S_1).[24–28] Recent studies further reveal that such parallel stacking in MR-TADF systems extends excited-state lifetimes and slows down emission processes, further limiting their practical utility.[29]

To circumvent these issues, emerging strategies have focused on hybrid molecular designs that combine the favorable features of both MR-TADF and conventional D–A–D architectures. Such frameworks aim to achieve a delicate balance: maintaining a narrow ΔE_{ST} while simultaneously suppressing detrimental π–π stacking and minimizing non-radiative decay. Recent works introduced a class of hybrid emitters that exhibit structural rigidity alongside controlled electronic separation, thereby mitigating ACQ without compromising efficiency.[12,30,31] Several recent studies have further expanded the design space. For example, flexible donor units combined with sulfoxide-locked acceptors leveraged intramolecular hydrogen bonding to restrict phenyl rotations and stabilize conformations.[32] Another approach demonstrated the synergistic integration of aggregation-induced emission (AIE) with TADF, which allowed fine-tuning of ΔE_{ST} and enabled efficient emission in both solution and solid state.[33] More recently, covalent incorporation of carbonyl and sulfoxide linkers was shown to enhance intramolecular interactions, suppress fragment rotations, and reduce non-radiative decay, thereby improving photophysical stability and device performance.[34] Nevertheless, even these rigid hybrids can exhibit residual aggregation effects, and the synthesis of fully fused backbones often demands more complex, multi-step routes compared to the relatively modular construction of D–A–D-type molecules.

In a complementary approach, Cheng *et al.* proposed a novel design paradigm in which donor and acceptor moieties are arranged in spatially well-separated geometries, enabling charge transfer to occur through space rather than *via* conventional conjugated pathways.[35,36] This strategy effectively minimizes HOMO–LUMO overlap, helping to maintain a small ΔE_{ST}, while also suppressing undesired π–π stacking interactions that often plague planar MR-TADF systems. As a result, such through-space charge-transfer (TSCT) architectures offer an attractive alternative to conventional TADF designs by combining structural rigidity, spectral stability, and high quantum efficiencies. However, this design strategy, while promising, raises a fundamental question: Is through-space charge transfer alone sufficient to ensure efficient TADF emission? Furthermore, the full exploration of chemical space encompassing all donor and acceptor moieties reported in such systems remains a significant challenge. Gaining more profound insight into the structure–property relationships that govern the photophysical performance of TSCT molecules is essential to guide rational emitter design. In particular, the influence of molecular symmetry on excited-state dynamics requires thorough investigation to determine whether symmetric frameworks yield advantages over asymmetric ones. A comparative assessment of D–A–D *versus* A–D–A topologies within a rigid framework is needed to establish generalizable design rules for maximizing RISC rates and optimizing emission efficiency in TADF systems.

To address these open questions and elucidate key structure–property correlations, the present study systematically investigates a chemically diverse set of TADF emitters. We explore a library of 21 carbazole-based molecules featuring both D–A–D and A–D–A configurations, with variations in donor identity, acceptor positioning, and molecular symmetry. Among these, three compounds have already been synthesized and characterized experimentally,[35,36] offering benchmarks for validating our computational methodology. Our results reveal that the spatial separation of frontier orbitals in these molecules consistently leads to small ΔE_{ST}, favorable oscillator strengths, and high radiative decay rates—features that collectively point toward efficient TADF activity. Notably, the charge-transfer process in these molecules occurs predominantly through space rather than through extended conjugation, providing further support for the TSCT design paradigm.

This work offers a comprehensive theoretical framework for understanding how molecular topology, symmetry, and orbital arrangement collectively influence TADF behavior in rigid, carbazole-based systems. By bridging design concepts from MR-TADF and TSCT architectures, our study identifies key structure–property trends that enable the simultaneous realization of small ΔE_{ST}, high PLQY, and suppressed non-radiative losses. The novelty of our approach lies in the systematic comparison of symmetric *versus* asymmetric motifs across both D–A–D and A–D–A frameworks, focusing on uncovering general principles that transcend specific chemical structures. These insights pave the way for the rational design of next-generation TADF emitters tailored for high-efficiency OLED applications.

2. Methods

The molecular structures examined in this study are illustrated in Fig. 1. The design of the target compounds draws inspiration from the through-space charge-transfer architectures recently proposed by Cheng *et al.*,[35,36] incorporating key structural motifs known to facilitate TADF behavior. Electron-donating groups such as methoxy and *N,N,N*-triphenylamine were selected for their strong donor characteristics while nitrogen-containing phenyl rings were employed as electron-accepting units to promote spatial orbital separation. To suppress undesirable π–π stacking and aggregation-caused quenching, sterically bulky *tert*-butyl substituents were strategically introduced. Among the various bridging units reported for TSCT-TADF emitters—such as phenyl rings, oxygen or sulfur linkers, and fully fused polycyclic scaffolds—the carbazole moiety offers a

Open Access Article. Published on 28 August 2025. Downloaded on 4/29/2026 2:04:37 AM.
This article is licensed under a Creative Commons Attribution-NonCommercial 3.0 Unported Licence.

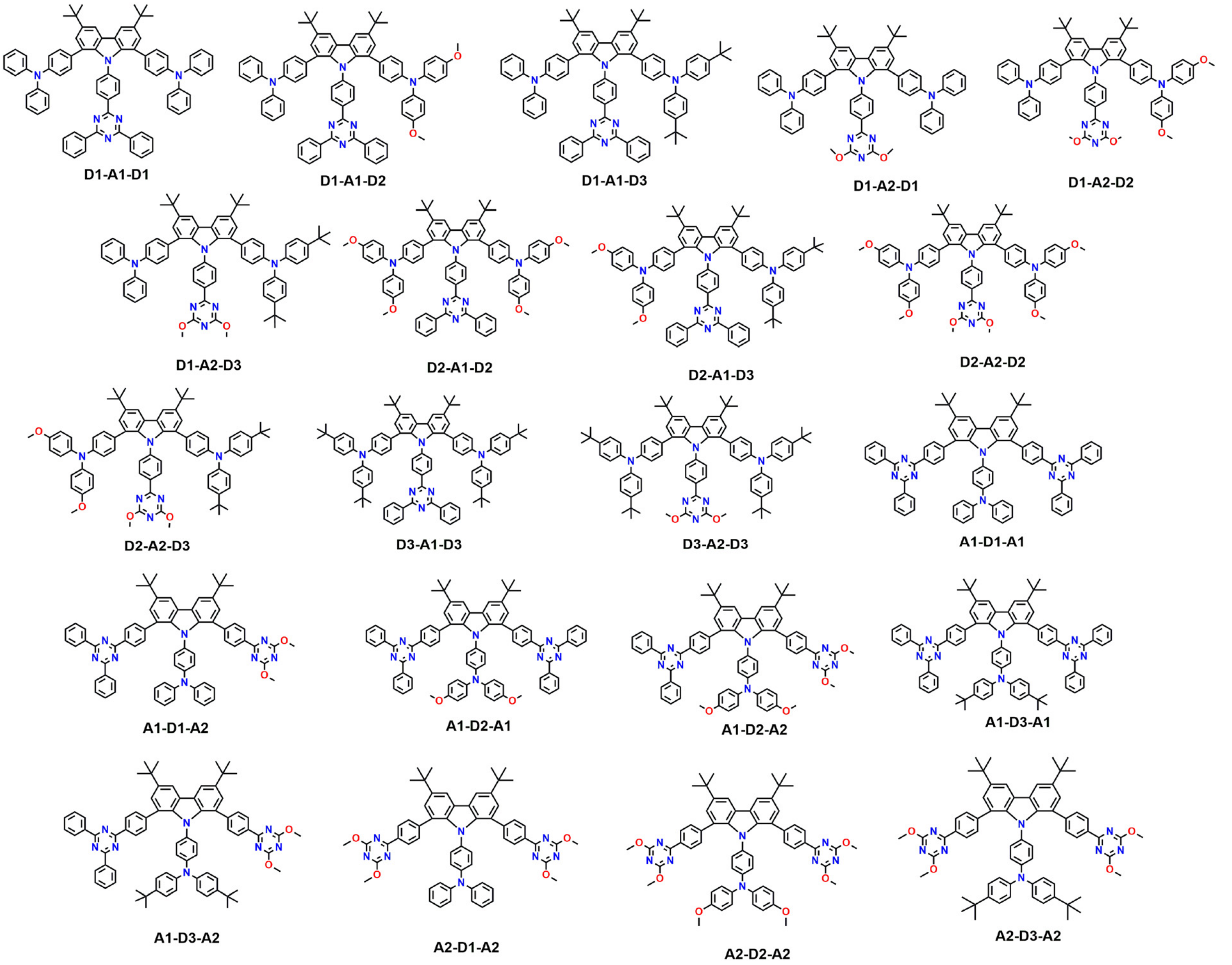

Fig. 1 Chemical structures of the 21 investigated TADF compounds comprising both symmetric and asymmetric architectures. The molecules are constructed using various combinations of three donor and two acceptor fragments, incorporating *tert*-butyl substitutions to suppress aggregation.

unique combination of rigidity, non-planarity, and synthetic accessibility. While phenyl bridges can provide spatial separation of HOMO and LUMO, they often retain greater conformational flexibility. Heteroatom linkers (O, S) enable electronic fine-tuning but may introduce rotational degrees of freedom, increasing non-radiative losses. Fully fused architectures deliver high rigidity yet can promote π–π stacking and aggregation-caused quenching. In contrast, carbazole effectively enforces donor–acceptor spatial separation, supports efficient through-space charge transfer, and suppresses parallel stacking—attributes that are central to the present molecular design strategy.

A total of 21 molecules were systematically constructed and analyzed, encompassing both symmetric and asymmetric configurations with varying donor–acceptor topologies. The molecular library spans combinations of three donor units and two acceptor fragments, as detailed in Fig. S1 of the SI. This set was designed to explore the influence of structural symmetry and substitution patterns on the photophysical properties relevant to TADF performance.

2.1. QM calculations

All quantum chemical calculations were performed using the ORCA v.5.0.3 software package.[37] Ground-state geometries (S_0) were optimized using the B3LYP exchange–correlation functional in conjunction with the 6-31G(d) basis set. Dispersion interactions were accounted for using Grimme's D3 correction with Becke–Johnson damping (D3BJ).[38] The B3LYP functional with D3 dispersion correction and the 6-31G(d) basis set offers a reliable balance between computational efficiency and accuracy, particularly for large organic molecules exceeding 200 atoms. This level of theory has been widely validated in previous studies of TADF emitters and is well-suited for capturing key photophysical properties relevant to the present work.[35,36,39] Solvent effects were included through the conductor-like polarizable continuum model (CPCM), with toluene (ε = 2.3741) as the implicit solvent medium. Following geometry optimization, single-point time-dependent DFT (TD-DFT) calculations were performed on the optimized structures to compute vertical excitation energies of the lowest five singlet (S_1–S_5) and triplet (T_1–T_5) states. Spin–orbit coupling (SOC) matrix elements between the singlet and triplet manifolds were evaluated at this level to facilitate the estimation of intersystem crossing (ISC) and reverse intersystem crossing rates. The radiative decay rate (k_{PF}) was computed using the Einstein spontaneous emission formula,[40] which relates oscillator strength to transition energy. Intersystem processes were modeled

Open Access Article. Published on 28 August 2025. Downloaded on 4/29/2026 2:04:37 AM.
This article is licensed under a Creative Commons Attribution-NonCommercial 3.0 Unported Licence.

using Fermi's Golden rule,[41,42] where the rates depend on both the SOC elements and energy gaps between relevant states. For ISC and RISC rates, we employed the semi-classical Marcus expression,[41,42] which neglects vibrational reorganization effects and assumes weak coupling. While this simplification omits electron–phonon interactions, it remains widely accepted in the TADF literature due to its computational efficiency and reasonable accuracy for qualitative and semi-quantitative analysis.[43,44] We analyzed the charge transfer character using the Multiwfn program to understand the nature of the excited states further.[45] Specifically, we computed the charge transfer number and the centroid distance between electron-donating and electron-accepting regions, extracted from the density difference plots. These plots, which visualize the redistribution of electron density upon excitation, were rendered using the VESTA software package.[46] Together, these analyses provide insight into the spatial characteristics and through-space *versus* through-bond nature of electronic excitations in the studied systems.

2.2. Analytical simulations

The protocol used for numerical simulations follows the framework established initially by Blom *et al.*[47] and subsequently adopted in our earlier studies.[12] These simulations were used to estimate the photoluminescence quantum yields and time-resolved exciton decay profiles by solving coupled rate equations incorporating radiative, non-radiative, ISC, and RISC channels. All equations used for calculating rate constants—radiative, ISC, and RISC—are provided in the SI, along with a detailed description of the simulation assumptions, number of states considered, and initial exciton population.

2.3. Molecular dynamics simulations

To further understand the bulk morphology and compare the structural characteristics of A–D–A and D–A–D architectures, molecular dynamics (MD) simulations were carried out on two representative compounds: **A1–D1–A1** and **D1–A1–D1**. The simulations were performed using the GROMACS software package,[48,49] and the resulting trajectories and final morphologies from the production runs were subjected to detailed structural analysis. To assess conformational stability and flexibility, we evaluated several structural metrics, including dihedral angle distributions, bond angle fluctuations, root-mean-square deviations (RMSD), and the time evolution of donor–acceptor distances. These analyses provide insights into the dynamic behavior of the two molecular topologies under ambient conditions. Additional details regarding the MD simulation setup and protocols are provided in the SI.

3. Results and discussion

As already highlighted, 21 TADF molecules were designed using various donor and acceptor fragment combinations, as shown in Fig. S1. Among these, 18 are newly proposed compounds, while three molecules have already been synthesized and experimentally studied in previous reports.[35,36] For naming consistency, we adopted a systematic nomenclature based on molecular topology: molecules with acceptor–donor–acceptor configuration are labeled as Ax–Dy–Az, and those with donor–acceptor–donor configuration as Dx–Ay–Dz, where the subscripts denote the specific donor or acceptor fragment used. This scheme includes both symmetric (*e.g.*, Ax–Dy–Ax or Dx–Ay–Dx) and asymmetric (*e.g.*, Ax–Dy–Az or Dx–Ay–Dz) structures. To validate the reliability of our computational methodology, we compared the calculated singlet–triplet energy gaps (ΔE_{ST}) and emission wavelengths with available experimental data for the three known compounds.[35,36] A side-by-side comparison is provided in Table S1. The close agreement between the computed and experimental values of ΔE_{ST}, emission wavelength, and photoluminescence quantum yield confirms the robustness and predictive accuracy of the computational framework used in this study.

3.1. Photophysical parameters

The key photophysical properties of the studied TADF emitters—including the singlet–triplet energy gap (ΔE_{ST}), spin–orbit coupling matrix elements $\left(H_{SO}^{S_1T_1}\right)$, emission wavelengths ($\lambda$), and oscillator strengths (f)—are summarized in Table 1. As evident from the data, all 21 molecules exhibit characteristically small ΔE_{ST} values, consistent with their through-space charge-transfer character arising from the spatial separation of donor and acceptor orbitals. Among the set, the smallest gap is observed for the **A1–D3–A1** molecule (0.001 eV), while **D2–A2–D2** stands out with the largest value (0.280 eV), reflecting a more localized excitation in the latter. Overall, A–D–A topologies (*e.g.*, **A1–D3–A1**, **A1–D2–A1**, **A1–D3–A2**) tend to yield lower ΔE_{ST} values than their D–A–D counterparts, likely due to enhanced symmetry in the acceptor environment and more effective TSCT pathways. Interestingly, molecular symmetry does not uniformly correlate with smaller gaps—**D2–A2–D2**, despite being symmetric, shows a significantly large gap. This anomaly suggests that electronic localization in both donor and acceptor units can outweigh the benefits of symmetry in minimizing ΔE_{ST}.

The spin–orbit coupling elements range from 0.009 cm^{-1} (**D2–A1–D3**) to 0.3 cm^{-1}. These values are comparable to those observed in other reported TADF systems[11,12,43,44,50] and indicate that efficient intersystem crossing and reverse intersystem crossing are feasible across this molecular set. Despite its large ΔE_{ST}, **D2–A2–D2** exhibits the highest SOC, which may partially compensate for its poor energetic alignment in TADF processes. The calculated emission wavelengths, evaluated in a toluene dielectric environment, span a wide range from deep blue (**D2–A2–D2**, 405 nm) to golden-yellow emission (**D2–A1–D3**, 572 nm), confirming the tunability of emission properties through a strategic donor–acceptor selection. As expected, a trade-off often exists between small ΔE_{ST} and oscillator strength due to reduced orbital overlap in charge-transfer transitions. However, several compounds—including **D1–A2–D1**, **D1–A2–D3**, **D2–A2–D3**, and **A2–D1–A2**—simultaneously exhibit high oscillator strengths ($!f > 0.2$) and moderate ΔE_{ST}, identifying them as promising

Open Access Article. Published on 28 August 2025. Downloaded on 4/29/2026 2:04:37 AM.
This article is licensed under a Creative Commons Attribution-NonCommercial 3.0 Unported Licence.

Table 1 Photophysical properties of the studied TADF molecules. ΔE_{ST} denotes the singlet–triplet energy gap (eV), $H_{SO}^{S_1T_1}$ is the spin–orbit coupling matrix element (cm^{-1}), λ is the emission wavelength (nm), and f is the oscillator strength. k_{PF} represents the fluorescence rate constant (10^7 s^{-1}), while k_{RISC}, k_{ISC}, and k_{TADF} correspond to reverse intersystem crossing, intersystem crossing, and TADF rate constants, respectively (10^5 s^{-1})

Compound	ΔE_{ST}	$H_{SO}^{S_1T_1}$	λ	f	k_{PF}	k_{RISC}	k_{ISC}	k_{TADF}
D1–A1–D1	0.017	0.109	512	0.013	0.35	8.46	49.00	6.80
D1–A1–D2	0.013	0.028	528	0.009	0.21	0.60	2.96	0.58
D1–A1–D3	0.026	0.042	540	0.107	3.87	0.99	8.14	0.99
D1–A2–D1	0.034	0.029	433	0.318	18.0	0.41	4.55	0.41
D1–A2–D2	0.037	0.024	482	0.146	7.69	0.26	3.20	0.26
D1–A2–D3	0.039	0.073	489	0.412	23.1	2.18	29.50	2.18
D2–A1–D2	0.023	0.033	574	0.127	4.35	0.67	4.87	0.67
D2–A1–D3	0.026	0.009	572	0.131	4.60	0.04	0.35	0.04
D2–A2–D2	0.280	0.300	405	0.117	1.91	0.002	31.20	0.002
D2–A2–D3	0.031	0.042	526	0.325	17.4	0.88	8.73	0.88
D3–A1–D3	0.019	0.013	543	0.021	0.54	0.12	0.76	0.12
D3–A2–D3	0.028	0.024	499	0.203	10.8	0.33	2.90	0.33
A1–D1–A1	0.013	0.022	506	0.170	6.72	0.37	1.84	0.37
A1–D1–A2	0.021	0.051	510	0.142	5.78	1.67	11.30	1.66
A1–D2–A1	0.009	0.022	570	0.160	6.33	0.41	1.72	0.41
A1–D2–A2	0.007	0.013	520	0.017	0.75	0.16	0.62	0.16
A1–D3–A1	0.001	0.117	499	0.184	7.33	13.70	42.70	13.40
A1–D3–A2	0.003	0.017	492	0.118	4.73	0.29	0.97	0.29
A2–D1–A2	0.047	0.041	435	0.215	9.93	0.55	10.20	0.55
A2–D2–A2	0.029	0.037	463	0.188	9.01	0.73	6.77	0.73
A2–D3–A2	0.011	0.033	448	0.179	10.20	0.88	4.01	0.87

candidates for efficient TADF emitters. Their combination of desirable photophysical attributes suggests a favorable balance between radiative efficiency and triplet harvesting, which is key to achieving high-performance OLED devices.

3.2. Radiative and non-radiative rates

Building on the photophysical characterization, we next evaluated the radiative and non-radiative decay rates to assess the emissive efficiency of the designed TADF emitters. The expressions used for calculating these rates, including k_{PF}, k_{ISC}, k_{RISC}, and k_{TADF}, are provided in the SI. These rates were derived using established formalisms, including Marcus theory for spin–flip transitions, and all computed values are summarized in Table 1. For the majority of molecules, fluorescence rate constants (k_{PF}) lie in the range of 10^7–10^8 s^{-1}, consistent with efficient radiative decay. The RISC rates (k_{RISC}) are typically on the order of 10^4–10^5 s^{-1}, while ISC rates (k_{ISC}) are generally one to two orders of magnitude higher, reflecting the favorable kinetics of singlet-to-triplet downconversion. The overall TADF rate (k_{TADF}), governed by both k_{PF} and k_{RISC}, is primarily limited by the latter, as RISC remains the rate-determining step in most TADF processes. A graphical comparison of ISC and RISC rates is shown in Fig. 2 for visual clarity. Despite the modest RISC rates, many compounds exhibit appreciable TADF behavior. This can be attributed to their minimal ΔE_{ST} values, which enable efficient thermal upconversion from the triplet to the singlet manifold. As a result, excitons are effectively recycled into radiative singlet emission pathways. One notable outlier is **D2–A2–D2**, which features a significantly larger ΔE_{ST} (0.28 eV). The associated energy mismatch results in a substantial imbalance between its RISC and ISC rates, thereby suppressing TADF efficiency relative to other dataset members. This observation underscores the importance of minimizing ΔE_{ST} to ensure optimal upconversion dynamics and high quantum yield in TADF systems.

3.3. Exciton characteristics

Following the rate calculations, we examined the excitonic characteristics of the first singlet excited state (S_1) to better

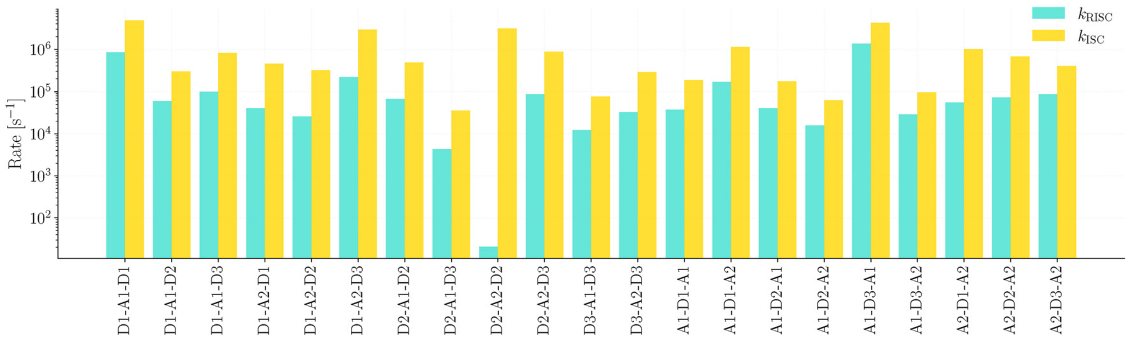

Fig. 2 Comparison of intersystem crossing (k_{ISC}) and reverse intersystem crossing (k_{RISC}) rates for the investigated TADF compounds. The plot highlights the kinetic asymmetry between downward and upward spin–flip processes and underscores the influence of ΔE_{ST} on RISC efficiency.

© 2025 The Author(s). Published by the Royal Society of Chemistry

Open Access Article. Published on 28 August 2025. Downloaded on 4/29/2026 2:04:37 AM.
This article is licensed under a Creative Commons Attribution-NonCommercial 3.0 Unported Licence.

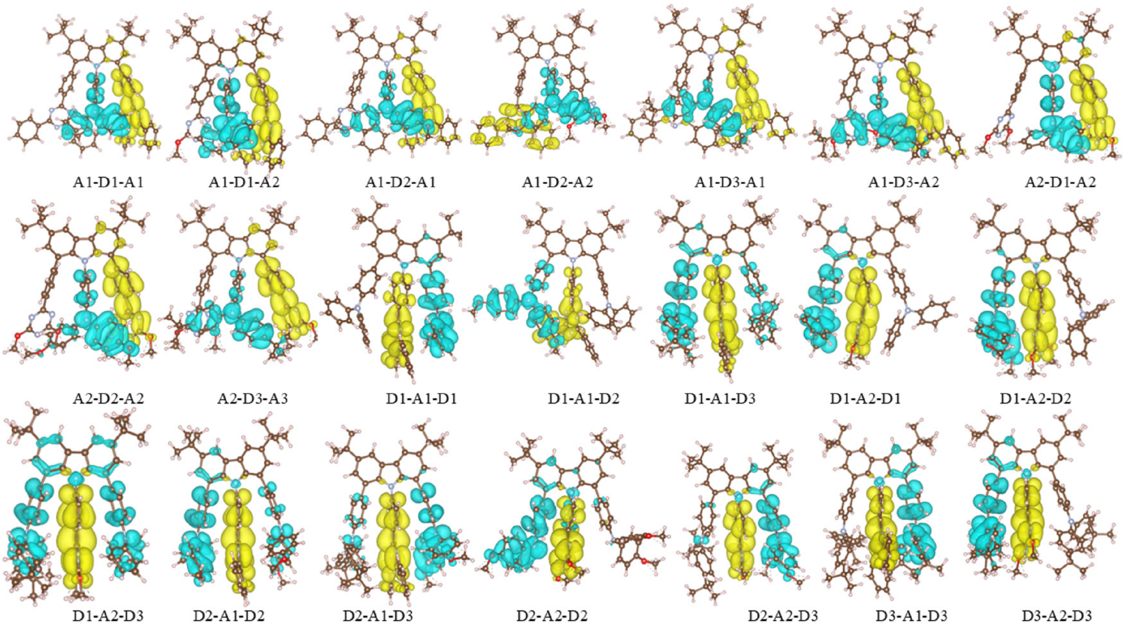

Fig. 3 Density difference plots for the S_1 to S_0 transition of the investigated compounds, rendered with an isovalue of 0.02 a.u. The blue regions represent areas of electron depletion (donor), while the yellow regions indicate electron accumulation (acceptor), illustrating the direction of intramolecular charge transfer upon excitation.

understand the nature of the emissive transitions in the studied molecules. Both qualitative and quantitative analyses were carried out to capture the spatial behavior of excited-state charge redistribution. Fig. 3 shows the electron density difference plots corresponding to the transition from the excited singlet state (S_1) to the ground state (S_0). These plots were generated using the relation $\Delta = \rho_{\text{ex}} - \rho_0$, where ρ_{ex} and ρ_0 are the electron densities of the excited and ground states, respectively. In these plots, yellow regions indicate electron depletion (hole density), and blue regions represent electron accumulation. The spatial separation between these regions reveals the charge transfer direction, with electrons moving from donor (blue) to acceptor (yellow) fragments. A striking feature in most cases is the minimal orbital overlap between donor and acceptor units, reflecting the through-space nature of the charge transfer (CT) process. This spatial decoupling is consistent with the extremely low singlet–triplet energy gaps observed previously and further confirms the long-range intramolecular CT behavior that underpins thermally activated delayed fluorescence in these systems.

Table 2 Photoluminescence quantum yields (PLQYs) and charge-transfer descriptors of the studied TADF emitters. Q_{CT} denotes the amount of charge transferred, d_{CT} represents the electron–hole centroid distance (in Å), and $S_\pm$ is the spatial overlap integral between electron and hole densities. PLQY values are reported as percentages

Compound	PLQY (%)	Q_{CT}	D_{CT}	$S_\pm$
D1–A1–D1	83.61	0.974	4.202	0.304
D1–A1–D2	97.31	0.981	5.399	0.182
D1–A1–D3	99.74	0.957	3.220	0.601
D1–A2–D1	99.98	0.955	3.727	0.333
D1–A2–D2	99.97	0.944	3.692	0.174
D1–A2–D3	99.91	0.949	1.750	0.561
D2–A1–D2	99.85	0.954	2.677	0.655
D2–A1–D3	99.99	0.953	3.215	0.608
D2–A2–D2	100.00	0.790	4.392	0.575
D2–A2–D3	99.95	0.959	3.212	0.501
D3–A1–D3	99.78	0.965	4.259	0.313
D3–A2–D3	99.97	0.963	3.836	0.319
A1–D1–A1	99.94	0.972	4.694	0.221
A1–D1–A2	99.71	0.969	3.744	0.381
A1–D2–A1	99.94	0.977	4.802	0.182
A1–D2–A2	99.79	0.985	6.490	0.246
A1–D3–A1	98.20	0.989	4.951	0.108
A1–D3–A2	99.94	0.984	5.367	0.123
A2–D1–A2	99.94	0.939	3.620	0.379
A2–D2–A2	99.92	0.958	3.967	0.306
A2–D3–A2	99.91	0.973	5.396	0.150

To complement the visual analysis, we quantitatively assessed three commonly used charge-transfer descriptors: the amount of transferred charge (Q_{CT}), the electron–hole centroid distance (D_{CT}), and the spatial overlap integral ($S_\pm$). Recent literature has extensively employed these parameters to distinguish between locally excited (LE), short-range CT, and long-range CT states.[43,44,50] The charge transfer number ranges between 0 and 1, with values closer to 1 indicating a stronger CT character. The centroid distance measures the physical separation between the centers of positive and negative charge densities, with values above 1.6 Å generally indicating long-range CT. In contrast, the spatial overlap parameter quantifies how much the electron and hole densities spatially coincide—larger values (approaching 1) suggest LE character, while smaller values reflect spatially separated CT states. The computed excitonic descriptors for all 21 compounds are presented in Table 2. As seen from the data, nearly all molecules exhibit high Q_{CT} values (>0.94) and large D_{CT} values (>3 Å), consistent with long-range charge-transfer behavior. Several compounds, including **A1–D3–A1** and **A1–D2–A2**, exhibit extreme CT character with $Q_{\text{CT}} > 0.98$ and $D_{\text{CT}} > 5$ Å.

© 2025 The Author(s). Published by the Royal Society of Chemistry

Open Access Article. Published on 28 August 2025. Downloaded on 4/29/2026 2:04:37 AM.
This article is licensed under a Creative Commons Attribution-NonCommercial 3.0 Unported Licence.

The exciton analysis supports the conclusion that the studied TADF emitters operate primarily *via* long-range through-space charge transfer, with only a few exceptions exhibiting partial LE character. These insights offer a design rationale for future emitters by correlating structural motifs with excitonic behavior.

3.4. Space charge-transfer analysis

To gain deeper insight into the underlying charge transfer mechanism in the studied TADF molecules, we conducted a fragment-based analysis to determine whether the transfer is bond-mediated (through chemical bonds) or space-mediated (*via* non-bonded spatial interactions). In this framework, the central carbazole unit was designated as fragment 1, while the remaining structural units—typically comprising donor and acceptor moieties—were assigned as fragments 2, 3, and 4. Charge redistribution during excitation was then analyzed between various fragment pairs: 1 → 2, 1 → 3, 1 → 4, 2 → 3, and 3 → 4. This analysis complements our earlier qualitative observations from the electron density difference plots (Fig. 3), which revealed negligible charge redistribution on the carbazole bridge. The absence of pronounced positive (yellow) or negative (blue) density lobes on the carbazole fragment indicates its limited involvement in excitation. Instead, the primary charge redistribution occurs between spatially distant donor and acceptor fragments. This behavior confirms that the excitation does not proceed *via* conventional through-bond conjugation but is dominated by a long-range, through-space charge transfer mechanism. The quantitative fragment-based charge-transfer data, along with the computed percentages of charge-transfer (CT) and locally excited (LE) characters, are summarized in Table 3. Across both D–A–D and A–D–A architectures, the charge transferred between the carbazole bridge (fragment 1) and the other moieties is consistently negligible. In contrast, substantial charge movement is observed between fragments 2 and 3 and between fragments 3 and 4—despite the absence of direct covalent bonding. This result further reinforces the notion of a spatial, non-bonded excitation pathway. Finally, the CT and LE percentage analysis reveals that all systems exhibit a dominant charge-transfer character with minimal LE contributions. This finding aligns well with the earlier descriptors (Q_{CT}, D_{CT}, and $S_{\pm}$) and collectively confirms that the photophysical behavior of these carbazole-bridged systems is governed by long-range, space-mediated charge transfer rather than through-bond electronic communication.

3.5. Analytical-simulations

To complement our investigation, we carried out numerical photoexcitation simulations to analyze excitonic decay dynamics, estimate exciton lifetimes, and determine the photoluminescence quantum yields (PLQYs) of the studied TADF emitters. These simulations model the temporal evolution of exciton populations, assuming an initial exciton density of 10^{17} cm^{-3} entirely localized in the first singlet excited state (S_1). The rate constants computed earlier—such as fluorescence (k_{PF}), intersystem crossing (k_{ISC}), and reverse intersystem crossing (k_{RISC})—were employed to track population changes and evaluate the resulting PLQYs. Details of the simulation protocols and underlying assumptions are provided in the SI and references to our prior methodological work.[12,47,51] Fig. 4 presents the simulated time-dependent behavior of exciton populations. As shown in Fig. 4a, the decay of the singlet population exhibits a biphasic profile: an initial rapid component corresponding to prompt fluorescence, followed by a slower decay associated with delayed fluorescence. This behavior arises due to the interplay of radiative decay and non-radiative processes such as ISC and RISC. Fig. 4b captures the evolution of the triplet state population, which increases initially due to ISC from the singlet state and subsequently declines as RISC channels exciton back to the singlet manifold. Notably, the triplet lifetime is

Table 3 Fragment-based charge transfer analysis of the studied molecules. The table reports the amount of charge transferred between specific fragment pairs (1 → 2, 1 → 3, *etc.*), where fragment 1 corresponds to the central carbazole unit and the remaining fragments represent donor or acceptor moieties. CT (%) denotes the overall charge-transfer character, while LE (%) indicates the contribution from locally excited states

Compound	1 → 2	1 → 3	1 → 4	2 → 3	3 → 4	CT (%)	LE (%)
D1–A1–D1	−0.0073	0.0736	0.0008	0.8863	−0.0034	98.34	1.66
D1–A1–D2	0.0001	0.0122	−0.0035	0.0003	−0.9633	98.45	1.55
D1–A1–D3	−0.0014	0.0949	−0.0109	−0.0109	−0.7165	97.66	2.34
D1–A2–D1	0.0012	0.0961	−0.0221	0.0030	−0.8323	97.09	2.91
D1–A2–D2	0.0001	0.0122	−0.0035	0.0003	−0.9633	98.45	1.55
D1–A2–D3	−0.0058	0.1697	−0.0122	0.2696	−0.5001	97.53	2.47
D2–A1–D2	−0.0016	0.0868	−0.0121	0.1768	−0.6795	97.81	2.19
D2–A1–D3	−0.0131	0.0383	−0.0025	0.7477	−0.1552	97.11	2.89
D2–A2–D2	−0.0145	0.0285	−0.0033	0.7578	−0.1223	97.80	2.20
D2–A2–D3	−0.0175	0.0847	−0.0009	0.7796	−0.0793	97.76	2.24
D3–A1–D3	0.0011	0.1026	−0.0077	0.0063	−0.8439	97.59	2.41
D3–A2–D3	0.0011	0.1026	−0.0077	0.0063	−0.8439	97.59	2.41
A1–D1–A1	0.0212	−0.0496	−0.0003	−0.9001	0.0042	98.44	1.57
A1–D1–A2	0.0247	−0.0440	−0.0003	−0.9013	0.0006	97.88	2.12
A1–D2–A1	0.0060	−0.0497	−0.0002	−0.9168	0.0075	98.43	1.57
A1–D2–A2	0.0143	0.0001	0.0000	−0.9639	0.0005	98.40	1.60
A1–D3–A1	0.0003	−0.0469	−0.0001	−0.8414	0.0959	98.77	1.24
A1–D3–A2	0.0045	−0.0350	−0.0001	−0.9435	0.0007	98.65	1.35
A2–D1–A2	−0.0011	−0.0838	0.1340	−0.0003	0.7198	95.87	4.19
A2–D2–A2	−0.0006	−0.1103	0.0167	−0.0009	0.8358	97.15	2.85
A2–D3–A2	−0.0003	−0.1042	0.0171	−0.0003	0.8595	98.47	1.53

© 2025 The Author(s). Published by the Royal Society of Chemistry

Open Access Article. Published on 28 August 2025. Downloaded on 4/29/2026 2:04:37 AM.
This article is licensed under a Creative Commons Attribution-NonCommercial 3.0 Unported Licence.

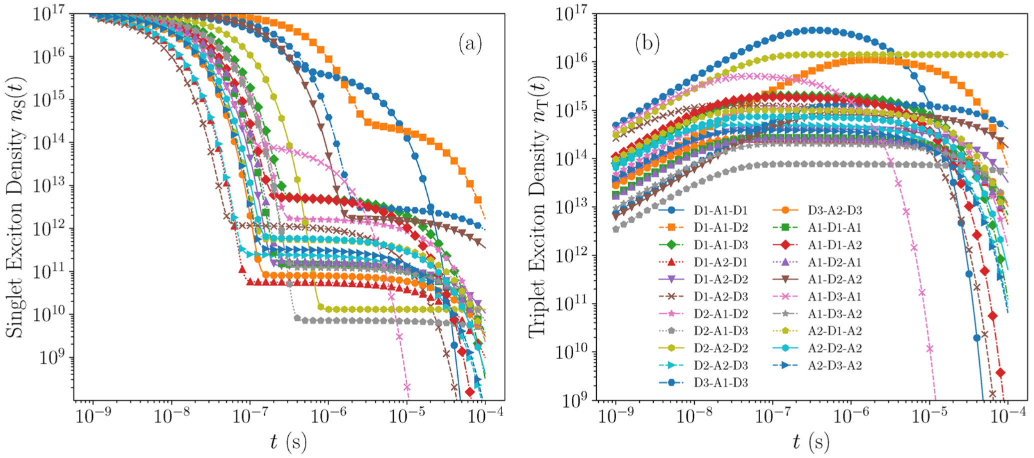

Fig. 4 Time-resolved exciton population dynamics simulated for the studied TADF molecules. (a) Temporal evolution of the singlet exciton population, exhibiting a fast prompt fluorescence decay followed by a slower delayed fluorescence component due to reverse intersystem crossing. (b) Corresponding triplet exciton dynamics show an initial rise from intersystem crossing and a gradual decay governed by RISC-mediated upconversion.

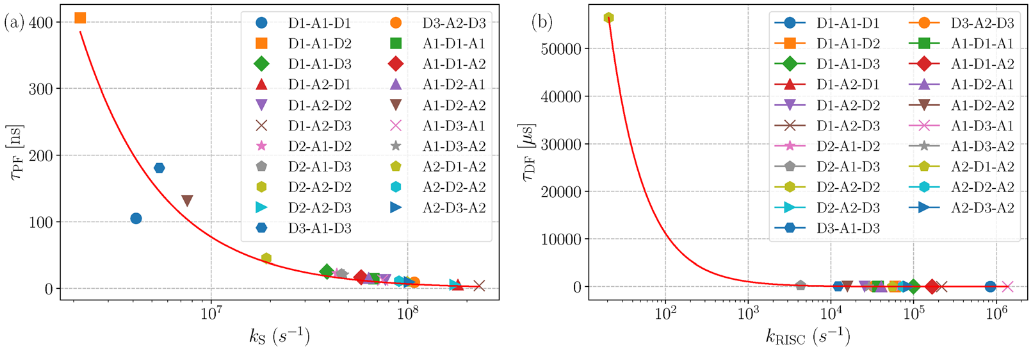

Fig. 5 Correlation between exciton lifetimes and photophysical rate constants in TADF systems. (a) The inverse relationship between prompt fluorescence lifetime and radiative fluorescence rate (k_{PF}) highlights that higher k_{PF} leads to shorter singlet lifetimes. (b) The inverse relationship between delayed fluorescence lifetime and reverse intersystem crossing rate (k_{RISC}) emphasizes the kinetic control of delayed emission by the RISC process.

significantly longer than the singlet's, consistent with the slower RISC kinetics compared to radiative decay.

All studied molecules exhibit exceptionally high PLQY values, with most approaching 100%, as summarized in Table 2. The only exception is **D1–A1–D1**, showing a slightly reduced PLQY of 83.6%. These high efficiencies can be attributed to minimized non-radiative losses, enabled by small singlet–triplet energy gaps (ΔE_{ST}), favorable spin–orbit coupling strengths, and balanced ISC/RISC rates that facilitate efficient exciton recycling between singlet and triplet states. Further insight into the exciton decay behavior is provided in Fig. 5. Fig. 5a demonstrates the inverse correlation between the radiative fluorescence rate (k_{PF}) and prompt fluorescence decay time—compounds with higher k_{PF} exhibit shorter singlet lifetimes. Similarly, Fig. 5b shows that higher RISC rates (k_{RISC}) correspond to faster-delayed fluorescence decay, emphasizing the role of spin–flip processes in determining delayed emission kinetics.

In summary, these simulation results confirm the superior photophysical performance of the investigated TADF emitters. Nearly unity PLQY, ultralow ΔE_{ST} values, and favorable exciton dynamics collectively point toward highly efficient thermally activated delayed fluorescence. Combined with our earlier findings—including through-space charge transfer character and robust radiative/non-radiative kinetics—this study provides a comprehensive framework for the rational design of next-generation TADF materials.

3.6. Morphological analysis

To complement the photophysical and excitonic analyses, we also examined the molecular morphologies of representative compounds to understand how architectural motifs influence structural dynamics and potential charge transfer behavior. As detailed in the Methods section, two key architectures were selected for comparative molecular dynamics simulations: D–A–D (**D1–A1–D1**) and A–D–A (**A1–D1–A1**). To validate the force field and ensure the reliability of the MD-generated configurations, we analyzed the dipole moment distribution and density convergence of the D–A–D system, with results provided in the SI. As shown in Fig. S2a, the dipole moment distribution from the MD simulation is broad but predominantly lies within the

Open Access Article. Published on 28 August 2025. Downloaded on 4/29/2026 2:04:37 AM.
This article is licensed under a Creative Commons Attribution-NonCommercial 3.0 Unported Licence.

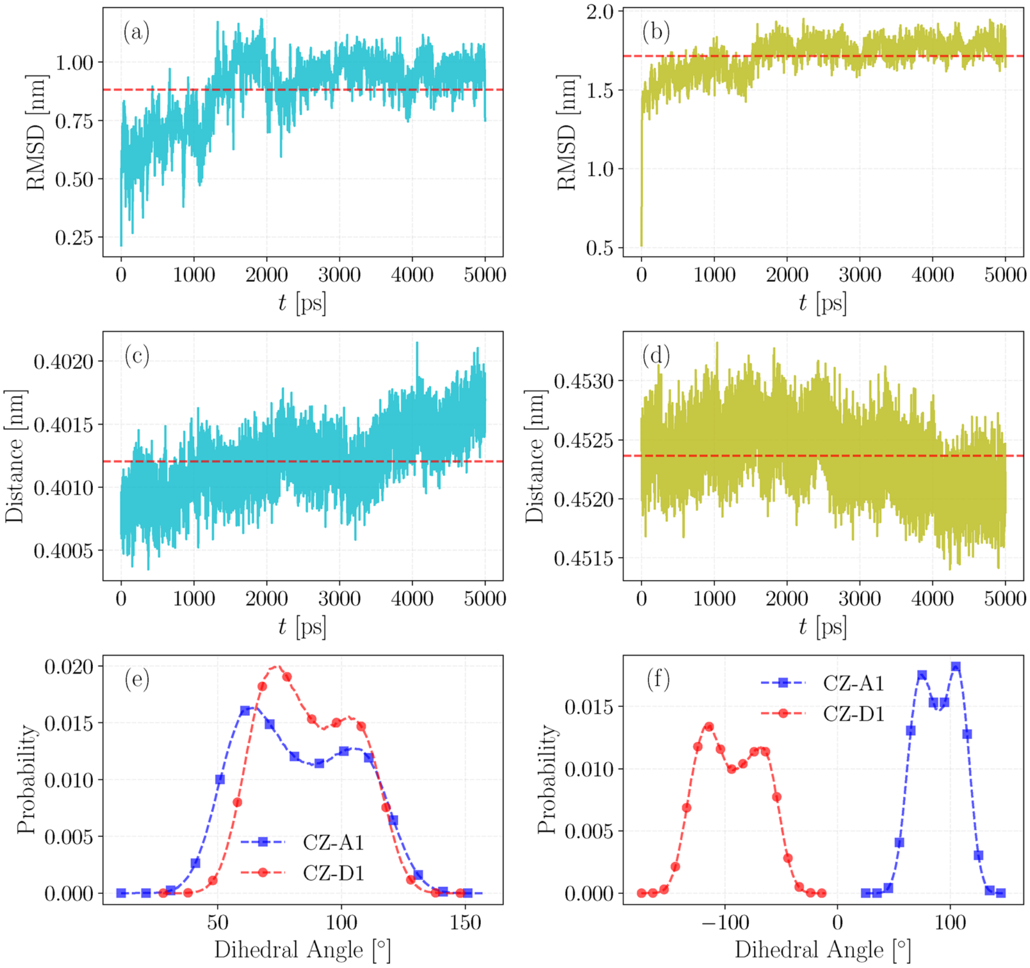

Fig. 6 Root-mean-square deviation (RMSD), donor–acceptor distance, and dihedral angle analyses from MD simulations of A–D–A and D–A–D molecules. Panels (a) and (b) show the RMSD of the entire molecule relative to its initial configuration for A–D–A and D–A–D, respectively. Panels (c) and (d) illustrate the time evolution of the distance between the centers of mass of the donor and acceptor units for A–D–A and D–A–D, respectively. Panels (e) and (f) display the distributions of dihedral angles between the carbazole and donor and carbazole and acceptor moieties for A–D–A and D–A–D, respectively.

1–2 Debye range, yielding an average value of 1.43 Debye. This average closely matches the quantum mechanical ground-state dipole moment of the **D1–A1–D1** molecule (1.33 Debye), indicating stable maintenance of the dipole moment near its quantum mechanical reference during the production run. Furthermore, Fig. S2b demonstrates the successful convergence of the density trajectory. Collectively, these results support the reliability and robustness of the OPLS force field[52–54] for morphological analysis of the investigated molecules.

Fig. 6 presents a comparative morphological analysis of the A–D–A and D–A–D systems. Specifically, it displays the root-mean-square deviation (RMSD) from the initial structure, donor–acceptor center-of-mass distance variations, and key dihedral angle distributions. As shown in Fig. 6a, the RMSD of **A1–D1–A1** is 0.88 nm, whereas **D1–A1–D1** exhibits a higher RMSD of 1.71 nm. When normalized by atom count (152 atoms for **A1–D1–A1** *vs.* 147 atoms for **D1–A1–D1**), the per-atom RMSDs are 0.006 nm and 0.012 nm, respectively, although both values lie within an acceptable range, the lower deviation for A–D–A suggests a slightly more rigid and stable structure—an important trait for minimizing nonradiative losses in optoelectronic applications. Fig. 6c and 6d compare the temporal evolution of donor–acceptor distances in the two systems. The A–D–A structure (**A1–D1–A1**) maintains a highly stable distance (0.4 nm) between donor and acceptor centers of mass. Similarly, the D–A–D structure shows a narrow range from 0.452 to 0.453 nm. These nearly invariant distances reinforce the conformational stability of both systems, with the shorter center-of-mass distance in **A1–D1–A1** suggesting more efficient through-space charge transfer.

Dihedral angle distributions between the carbazole and donor/acceptor moieties are shown in Fig. 6e and 6f. The dihedral angles cluster around 90° for both molecular types, indicating an orthogonal orientation between the carbazole and its adjacent groups. This perpendicular arrangement minimizes π-conjugation between donor and acceptor orbitals and supports a through-space charge transfer mechanism, consistent with earlier electronic structure analyses and the near-zero

Open Access Article. Published on 28 August 2025. Downloaded on 4/29/2026 2:04:37 AM.
This article is licensed under a Creative Commons Attribution-NonCommercial 3.0 Unported Licence.

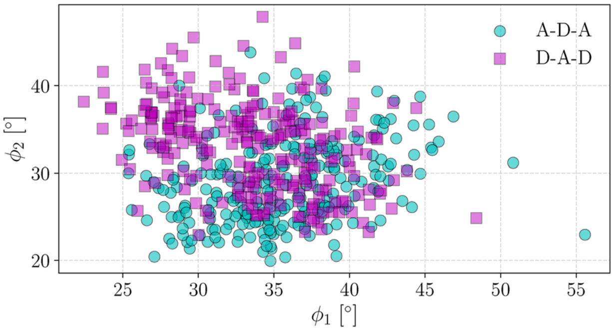

Fig. 7 Angle distribution between the centers of mass of the carbazole unit, the side moiety, and the central moiety for A–D–A and D–A–D architectures. The plot highlights distinct spatial arrangements, with A–D–A molecules predominantly occupying the lower-left region (narrower angles) and D–A–D molecules appearing more frequently in the upper-left region (wider angles). These distributions reflect structural differences influencing donor–acceptor separation and charge-transfer efficiency.

singlet–triplet energy gaps observed. To gain further geometric insights, we evaluated the angle formed by the centers of mass of the carbazole moiety, the central core, and the terminal group. The distribution of these angles is shown in Fig. 7. Notably, the A–D–A molecules predominantly populate the lower-left region of the distribution map, reflecting narrower angles, while D–A–D molecules are more prevalent in the upper-left region, corresponding to wider angles. These angular differences align with the donor–acceptor distances discussed earlier: A–D–A molecules exhibit a more compact geometry, whereas D–A–D molecules are slightly more extended. This subtle but consistent distinction between the two architectures underscores the geometric and electronic advantages of the A–D–A motif for efficient TADF behavior.

To further evaluate the structural robustness of the studied molecules, we calculated the bond dissociation energies (BDEs) of the potentially fragile bonds connecting the carbazole (CZ) unit to the donor (D1) and acceptor (A1) moieties. For the **D1–A1–D1** architecture, the BDE of the CZ–D1 bond was 6.19 eV, while that of the CZ–A1 bond was 5.34 eV. In contrast, the **A1–D1–A1** compound exhibited a BDE of 4.98 eV for the CZ–D1 bond and 6.11 eV for the CZ–A1 bond. These values are notably higher than those reported in our previous study,[12] suggesting that these bonds exhibit sufficient thermodynamic stability despite being labeled as potentially weak points. This mechanical resilience is crucial for maintaining high photoluminescence efficiency and long-term operational durability in TADF materials.

The structural arrangement of donor and acceptor fragments plays a decisive role in determining TADF performance. In the carbazole-embedded architectures studied here, the donor and acceptor units are spatially separated through the carbazole bridge rather than connected by flexible single bonds, as is typical in conventional D–A–D systems. This design restricts relative rotational motion between fragments, thereby suppressing non-radiative decay pathways while maintaining an ultralow singlet–triplet energy gap (approaching 0 eV). Additionally, the non-planar geometry imposed by the carbazole unit reduces the likelihood of parallel stacking in the solid state, mitigating H-type aggregation and associated emission quenching. The donor–acceptor distances observed in our optimized structures further support efficient charge-transfer behavior, with shorter separations enhancing electronic coupling and increasing the probability of exciton–hole recombination. These combined structural features contribute to the high predicted PLQYs and robust TADF characteristics observed across the designed molecules.

Moreover, from a device-performance standpoint, these structural metrics have important implications. The calculated BDE values for the bonds connecting the carbazole bridge to donor or acceptor fragments fall in the 4–6 eV range, substantially higher than those reported for certain conventional designs (*e.g.*, MR-TADF systems with strained ring linkages).[12] Such high BDEs indicate strong intrinsic chemical stability, suggesting that the emitters are likely to resist bond cleavage and degradation during prolonged operation. The RMSD values further support this robustness, showing minimal deviation from the initial structures over the simulation timescale. This conformational rigidity helps suppress non-radiative decay pathways and maintain high photoluminescence efficiency under repeated excitation–emission cycles, a prerequisite for long operational lifetimes in OLED devices. In addition, the donor–acceptor distances observed in both A–D–A and D–A–D architectures correlate with potential charge-transfer efficiency. The shorter donor–acceptor separation in A–D–A molecules enhances electronic coupling between frontier orbitals, increasing the probability of exciton–hole recombination and, consequently, emission efficiency. By linking these morphological parameters to stability and charge-transfer behavior, our results demonstrate that molecular architecture not only dictates photophysical properties but also offers predictive insight into the operational durability and performance of TADF-based OLEDs.

4. Conclusion

The present findings highlight that the interplay between molecular topology, frontier orbital distribution, and structural rigidity can be deliberately tuned to address the long-standing trade-offs in TADF emitter design. By comparing A–D–A and D–A–D frameworks within a carbazole-bridged through-space charge-transfer paradigm, this work identifies design principles that simultaneously favor small singlet–triplet gaps, efficient triplet harvesting, and mechanical robustness—attributes that are rarely achieved together.

Beyond the specific molecules studied here, the combined use of photophysical modelling, exciton dynamics, and morphological stability analysis offers a transferable computational protocol for screening next-generation TADF emitters before synthesis. The demonstrated link between donor–acceptor separation, conformational rigidity, and predicted device-level stability provides a foundation for tailoring materials not only

© 2025 The Author(s). Published by the Royal Society of Chemistry

Open Access Article. Published on 28 August 2025. Downloaded on 4/29/2026 2:04:37 AM.
This article is licensed under a Creative Commons Attribution-NonCommercial 3.0 Unported Licence.

for OLED efficiency but also for operational durability. More broadly, this work reinforces the value of integrating quantum chemical descriptors with dynamic structural analyses to move from "property matching" toward predictive, mechanism-driven emitter design. Such strategies can accelerate the discovery of stable, high-performance organic emitters across diverse device platforms, from displays to solid-state lighting.

Author contributions

AM conceived the problem. Sanyam and NT conducted all the simulations. Sanyam and AM analyzed the results and prepared the draft.

Conflicts of interest

There are no conflicts to declare.

Data availability

The data supporting this article, including computational details and supplementary figures, have been included as part of the SI. Supplementary information: Photophysical rates, analytical simulation, molecular dynamics simulation details, chemical structures of donor/acceptor fragments, a table of photophysical parameters, and dipole moment distribution and density convergence from MD trajectories. See DOI: **https://doi.org/10.1039/d5ma00731c**

Acknowledgements

The authors gratefully acknowledge the Indian Institute of Technology Gandhinagar, India, for providing research facilities and financial support. We thank PARAM Ananta for computational resources. We acknowledge Nikhitha R. for helpful discussions and assistance in setting up the analytical simulations.

References

1 A. Endo, K. Sato, K. Yoshimura, T. Kai, A. Kawada, H. Miyazaki and C. Adachi, Efficient up-conversion of triplet excitons into a singlet state and its application for organic light emitting diodes, *Appl. Phys. Lett.*, 2011, **98**, 083302.

2 H. Uoyama, K. Goushi, K. Shizu, H. Nomura and C. Adachi, Highly efficient organic light-emitting diodes from delayed fluorescence, *Nature*, 2012, **492**, 234–238.

3 Y. Xu, Z. Cheng, Z. Li, B. Liang, J. Wang, J. Wei, Z. Zhang and Y. Wang, Molecular-structure and device-configuration optimizations toward highly efficient green electroluminescence with narrowband emission and high color purity, *Adv. Opt. Mater.*, 2020, **8**, 1902142.

4 Y. Xu, C. Li, Z. Li, Q. Wang, X. Cai, J. Wei and Y. Wang, Constructing Charge-Transfer Excited States Based on Frontier Molecular Orbital Engineering: Narrowband Green Electroluminescence with High Color Purity and Efficiency, *Angew. Chem.*, 2020, **59**, 17442–17446.

5 Y. Liu, C. Li, Z. Ren, S. Yan and M. R. Bryce, All-organic thermally activated delayed fluorescence materials for organic light-emitting diodes, *Nat. Rev. Mater.*, 2018, **3**, 18020.

6 S. Izumi, H. F. Higginbotham, A. Nyga, P. Stachelek, N. Tohnai, P. d Silva, P. Data, Y. Takeda and S. Minakata, Thermally activated delayed fluorescent donor-acceptor-donor-acceptor π -conjugated macrocycle for organic light-emitting diodes, *J. Am. Chem. Soc.*, 2020, **142**, 1482–1491.

7 P. Stachelek, J. S. Ward, P. L. dos Santos, A. Danos, M. Colella, N. Haase, S. J. Raynes, A. S. Batsanov, M. R. Bryce and A. P. Monkman, Molecular Design Strategies for Color Tuning of Blue TADF Emitters, *ACS Appl. Mater. Interfaces*, 2019, **11**, 27125–27133.

8 K. Goushi, K. Yoshida, K. Sato and C. Adachi, Organic light-emitting diodes employing efficient reverse intersystem crossing for triplet-to-singlet state conversion, *Nat. Photonics*, 2012, **6**, 253–258.

9 Y. Zhang, D. Zhang, J. Wei, X. Hong, Y. Lu, D. Hu, G. Li, Z. Liu, Y. Chen and L. Duan, Achieving pure green electroluminescence with CIEy of 0.69 and EQE of 28.2% from an aza-fused multi-resonance emitter, *Angew. Chem.*, 2020, **132**, 17652–17656.

10 T. Hatakeyama, K. Shiren, K. Nakajima, S. Nomura, S. Nakatsuka, K. Kinoshita, J. Ni, Y. Ono and T. Ikuta, Ultrapure Blue Thermally Activated Delayed Fluorescence Molecules: Efficient HOMO-LUMO Separation by the Multiple Resonance Effect, *Adv. Mater.*, 2016, **28**, 2777–2781.

11 Sanyam, R. Khatua and A. Mondal, Constructing Multiresonance Thermally Activated Delayed Fluorescence Emitters for Organic LEDs: A Computational Investigation, *J. Phys. Chem. A*, 2023, **127**, 10393–10405.

12 R. Nikhitha and A. Mondal, Breaking the trade-off between and oscillator strength in hybrid LR/SR-CT compounds for enhanced TADF performance, *J. Mater. Chem. C*, 2025, **13**, 1893–1906.

13 F. Huang, K. Wang, Y.-Z. Shi, X.-C. Fan, X. Zhang, J. Yu, C.-S. Lee and X.-H. Zhang, Approaching Efficient and Narrow RGB Electroluminescence from D–A-Type TADF Emitters Containing an Identical Multiple Resonance Backbone as the Acceptor, *ACS Appl. Mater. Interfaces*, 2021, **13**, 36089–36097.

14 H. S. Kim, S. H. Lee, S. Yoo and C. Adachi, Understanding of complex spin up-conversion processes in charge-transfer-type organic molecules, *Nat. Commun.*, 2024, **15**, 2267.

15 M. Yang, I. S. Park and T. Yasuda, Full-Color, Narrowband, and High-Efficiency Electroluminescence from Boron and Carbazole Embedded Polycyclic Heteroaromatics, *J. Am. Chem. Soc.*, 2020, **142**, 19468–19472.

16 D. Hall, S. M. Suresh, P. L. dos Santos, E. Duda, S. Bagnich, A. Pershin, P. Rajamalli, D. B. Cordes, A. M. Z. Slawin, D. Beljonne, A. Köhler, I. D. W. Samuel, Y. Olivier and E. Zysman-Colman, Improving Processability and Efficiency of Resonant TADF Emitters: A Design Strategy, *Adv. Opt. Mater.*, 2020, **8**, 1901627.

© 2025 The Author(s). Published by the Royal Society of Chemistry

Open Access Article. Published on 28 August 2025. Downloaded on 4/29/2026 2:04:37 AM.
This article is licensed under a Creative Commons Attribution-NonCommercial 3.0 Unported Licence.

17 T. J. Penfold, E. Gindensperger, C. Daniel and C. M. Marian, Spin-vibronic mechanism for intersystem crossing, *Chem. Rev.*, 2018, **118**, 6975–7025.

18 X.-K. Chen, D. Kim and J.-L. Brédas, Thermally activated delayed fluorescence (TADF) path toward efficient electroluminescence in purely organic materials: molecular level insight, *Acc. Chem. Res.*, 2018, **51**, 2215–2224.

19 P. S. Rukin, M. Fortino, D. Prezzi and C. A. Rozzi, Complementing Adiabatic and Nonadiabatic Methods To Understand Internal Conversion Dynamics in Porphyrin Derivatives, *J. Chem. Theory Comput.*, 2024, **20**, 10759–10769.

20 D. Valverde, C. T. Ser, G. Ricci, K. Jorner, R. Pollice, A. Aspuru-Guzik and Y. Olivier, Computational Investigations of the Detailed Mechanism of Reverse Intersystem Crossing in Inverted Singlet-Triplet Gap Molecules, *ACS Appl. Mater. Interfaces*, 2024, **16**, 66991–67001.

21 J. Guan, C. Shen, J. Peng and J. Zheng, What leads to aggregation-induced emission?, *J. Phys. Chem. Lett.*, 2021, **12**, 4218–4226.

22 Y. Liu, L. Wang, L. Xu and Y. Song, From aggregation-caused quenching to aggregation-induced delayed fluorescence: the impact of the effect of substituents, *J. Mater. Chem. C*, 2023, **11**, 13403–13417.

23 J. He, H. Chen, J. Li, J. Wang, J. Xu, Z. Zhao and B. Z. Tang, Aggregation-induced delayed fluorescence molecules with mechanochromic behaviors for efficient blue organic light-emitting diodes, *Cell. Rep. Phys. Sci.*, 2022, **3**, 100733.

24 W. Zhang, S. Li, Y. Gong, J. Zhang, Y. Zhou, J. Kong, H. Fu and M. Zhou, Aggregation Enhanced Thermally Activated Delayed Fluorescence through Spin-Orbit Coupling Regulation, *Angew. Chem.*, 2024, **136**, e202404978.

25 P. Cen, J. Huang, C. Jin, J. Wang, Y. Wei, H. Zhang and M. Tian, Aggregation-induced emission luminogens for in vivo molecular imaging and theranostics in cancer, *Aggregate*, 2023, **4**, e352.

26 G. Feng and B. Liu, Aggregation-induced emission (AIE) dots: emerging theranostic nanolights, *Acc. Chem. Res.*, 2018, **51**, 1404–1414.

27 J. Gierschner, L. Luer, B. Milián-Medina, D. Oelkrug and H.-J. Egelhaaf, Highly emissive H-aggregates or aggregation-induced emission quenching? The photophysics of all-trans para-distyrylbenzene, *J. Phys. Chem. Lett.*, 2013, **4**, 2686–2697.

28 D. Rajput, Sanyam, G. Rawat, P. Sorout, S. Kanvah and A. Mondal, From Molecule to Aggregate: Understanding AIE through Multiscale Experimental and Computational Techniques, *J. Phys. Chem. B*, 2024, **128**, 12559–12570.

29 S. Kuila, H. Miranda-Salinas, J. Eng, C. Li, M. R. Bryce, T. J. Penfold and A. P. Monkman, Rigid and planar π-conjugated molecules leading to long-lived intramolecular charge-transfer states exhibiting thermally activated delayed fluorescence, *Nat. Commun.*, 2024, **15**, 9611.

30 G. Meng, H. Dai, Q. Wang, J. Zhou, T. Fan, X. Zeng, X. Wang and Y. Zhang, *et al.*, High-efficiency and stable short-delayed fluorescence emitters with hybrid long-and short-range charge-transfer excitations, *Nat. Commun.*, 2023, **14**, 2394.

31 H. L. Lee, J. Kang, J. Lim, S. C. Kim, S. O. Jeon and J. Y. Lee, Hybridization of short-range and long-range charge transfer excited states in multiple resonance emitter, *Nat. Commun.*, 2023, **14**, 4818.

32 J. Wang, Y. Niu, Y. Yang, H. Peng, J. Zhang and C. Yao, Towards efficient blue aggregation-induced emission and delayed fluorescence molecules by locking the skeleton of indolocarbazole derivatives for non-doped OLEDs, *Mater. Today Chem.*, 2024, **40**, 102239.

33 J. Wang, J. Zhang, C. Jiang, C. Yao and X. Xi, Effective design strategy for aggregation-induced emission and thermally activated delayed fluorescence emitters achieving 18% external quantum efficiency pure-blue OLEDs with extremely low roll-off, *ACS Appl. Mater. Interfaces*, 2021, **13**, 57713–57724.

34 J. Wang, Y. Yang, F. Gu, X. Zhai, C. Yao, J. Zhang, C. Jiang and X. Xi, Molecular Engineering Modulating the Singlet-Triplet Energy Splitting of Indolocarbazole-Based TADF Emitters Exhibiting AIE Properties for Nondoped Blue OLEDs with EQE of Nearly 20%, *ACS Appl. Mater. Interfaces*, 2023, **15**, 59643–59654.

35 K. Li, Y. Chen, B. Yao, K. Dou, T. Wang, H. Deng, H. Zhan, Z. Xie and Y. Cheng, Insight into through-space conjugation in rotation-restricted thermally activated delayed fluorescence compounds, *J. Mater. Chem. C*, 2022, **10**, 15152–15159.

36 K. Dou, K. Li, M. Chen, B. Zhao, Y. Chen, H. Deng, X. Liu and C. Zhao, *et al.*, Efficient thermally activated delayed fluorescence carbazole derivatives with a cofacial acceptor/donor/acceptor chromophore: comparable luminescent properties to their counterparts with the opposite configuration of donor/acceptor/donor, *J. Mater. Chem. C*, 2024, **12**, 12444–12450.

37 F. Neese, The ORCA program system, *Wiley Interdiscip. Rev.: Comput. Mol. Sci.*, 2012, **2**, 73–78.

38 L. Wittmann, I. Gordiy, M. Friede, B. Helmich-Paris, S. Grimme, A. Hansen and M. Bursch, Extension of the D3 and D4 London dispersion corrections to the full actinides series, *Phys. Chem. Chem. Phys.*, 2024, **26**, 21379–21394.

39 I. Y. Zhang, J. Wu and X. Xu, Extending the reliability and applicability of B3LYP, *Chem. Commun.*, 2010, **46**, 3057–3070.

40 K. Zhang, J. Liu, Y. Zhang, J. Fan, C.-K. Wang and L. Lin, Theoretical Study of the Mechanism of Aggregation-Caused Quenching in Near-Infrared Thermally Activated Delayed Fluorescence Molecules: Hydrogen-Bond Effect, *J. Phys. Chem. C*, 2019, **123**, 24705–24713.

41 S. Xu, Q. Yang, Y. Wan, R. Chen, S. Wang, Y. Si, B. Yang, D. Liu, C. Zheng and W. Huang, Predicting intersystem crossing efficiencies of organic molecules for efficient thermally activated delayed fluorescence, *J. Mater. Chem. C*, 2019, **7**, 9523–9530.

42 N. Aizawa, Y. Harabuchi, S. Maeda and Y.-J. Pu, Kinetic prediction of reverse intersystem crossing in organic donor-acceptor molecules, *Nat. Commun.*, 2020, **11**, 3909.

43 D. Hall, J. C. Sancho-Garca, A. Pershin, G. Ricci, D. Beljonne, E. Zysman-Colman and Y. Olivier, Modeling of multiresonant thermally activated delayed fluorescence emitters- properly

Open Access Article. Published on 28 August 2025. Downloaded on 4/29/2026 2:04:37 AM.
This article is licensed under a Creative Commons Attribution-NonCommercial 3.0 Unported Licence.

accounting for electron correlation is key!, *J. Chem. Theory Comput.*, 2022, **18**, 4903–4918.

44 Sanyam, R. Khatua and A. Mondal, Cost-Effective Approach for Modeling of Multiresonant Thermally Activated Delayed Fluorescence Emitters, *J. Chem. Theory Comput.*, 2023, **19**, 9290–9301.

45 T. Lu and F. Chen, Multiwfn: A multifunctional wavefunction analyzer, *J. Comput. Chem.*, 2012, **33**, 580–592.

46 K. Momma and F. Izumi, VESTA3 for three-dimensional visualization of crystal, volumetric and morphology data, *J. Appl. Crystallogr.*, 2011, **44**, 1272–1276.

47 Y. Li and P. W. Blom, Analytical description of the charge-to-photon conversion efficiency for electroluminescent devices based on thermally activated delayed fluorescence, *Phys. Rev. Appl*, 2024, **21**, 044037.

48 B. Hess, C. Kutzner, D. Van Der Spoel and E. Lindahl, GROMACS 4: algorithms for highly efficient, load-balanced, and scalable molecular simulation, *J. Chem. Theory Comput.*, 2008, **4**, 435–447.

49 S. Pronk, S. Páll, R. Schulz, P. Larsson, P. Bjelkmar, R. Apostolov, M. R. Shirts, J. C. Smith, P. M. Kasson, D. Van Der Spoel, B. Hess and E. Lindahl, GROMACS 4.5: a high-throughput and highly parallel open source molecular simulation toolkit, *Bioinformatics*, 2013, **29**, 845–854.

50 Sanyam, P. Sorout and A. Mondal, Rational Design of Organic Emitters with Inverted Singlet-Triplet Gaps for Enhanced Exciton Management, *J. Phys. Chem. A*, 2024, **128**, 7114–7123.

51 R. Scholz, P. Kleine, R. Lygaitis, L. Popp, S. Lenk, M. K. Etherington, A. P. Monkman and S. Reineke, Investigation of thermally activated delayed fluorescence from a donor-acceptor compound with time-resolved fluorescence and density functional theory applying an optimally tuned range-separated hybrid functional, *J. Phys. Chem. A*, 2020, **124**, 1535–1553.

52 W. L. Jorgensen and J. Tirado-Rives, The OPLS [optimized potentials for liquid simulations] potential functions for proteins, energy minimizations for crystals of cyclic peptides and crambin, *J. Am. Chem. Soc.*, 1988, **110**, 1657–1666.

53 W. L. Jorgensen, D. S. Maxwell and J. Tirado-Rives, Development and testing of the OPLS all-atom force field on conformational energetics and properties of organic liquids, *J. Am. Chem. Soc.*, 1996, **118**, 11225–11236.

54 W. L. Jorgensen and J. Tirado-Rives, Potential energy functions for atomic-level simulations of water and organic and biomolecular systems, *Proc. Natl. Acad. Sci. U. S. A.*, 2005, **102**, 6665–6670.

© 2025 The Author(s). Published by the Royal Society of Chemistry